

# Exploring Spectral Singularities in Dirac Semimetals: The Role of Non-Hermitian Physics and Dichroism

Mustafa Sarisaman\*

*National Intelligence Academy, Institute of Engineering and Science, Ankara, Turkey and  
Department of Physics, Istanbul University, 34134, Vezneciler, Istanbul, Turkey*

Murat Tas†

*Department of Physics, Gebze Technical University, 41400 Kocaeli, Turkey*

Enes Talha Kirca‡

*Department of Physics, Istanbul University, 34134, Vezneciler, Istanbul, Turkey*

In this study, motivated by recent advancements in non-Hermitian physics, we explore new characteristics of Dirac semimetals (DSMs) using the spectral singularities by means of scattering techniques, with the goal of uncovering additional unique properties. To achieve this, we investigate how the axion texture of a DSM affects its topological properties by analyzing its interaction with electromagnetic waves. We examine the transverse electric (TE) mode configuration, where the magneto-electric effect induces a dichroic property in these materials. This behavior is particularly interesting and commonly seen in potential DSM candidates. Consequently, we report for the first time that a dichroic DSM generates 12 unique topological laser types. We discover that surface currents are generated by topological terms on the surface of the DSM slab. Furthermore, we examine how the  $\theta$  term associated with axions in topological materials contributes to these topological properties. Our study reveals distinct topological role of the  $\theta$  term more clearly than ever before. Our results confirm that the topological properties of DSMs with a single Dirac cone remain stable under external influences and that a topologically robust DSM laser can be developed accordingly.

PACS numbers: 03.50.De, 03.65.-w, 03.65.Nk, 42.25.Bs, 42.25.Gy, 42.55.-f, 71.55.Ak, 78.20.-e, 81.05.Bx

## INTRODUCTION

It is fascinating to discover that certain advanced mathematical concepts, such as topology, have direct physical counterparts with practical applications [1, 2]. This realization has opened up new avenues for research, particularly in understanding topological phases of matter and their integration into material science, giving rise to novel application areas [3–5]. Among various topological materials that have been identified, some of the most prominent include electronic and photonic topological insulators, topological superconductors, and Dirac and Weyl semimetals and metals [6–18]. One class of materials that has garnered significant attention recently is the topological Dirac semimetals (DSMs), where the valence and conduction bands touch at specific points in momentum space, known as Dirac points [19–30]. What distinguishes these materials as “topological” is the unique arrangement of degenerate Weyl nodes that act as an axion term, imparting a topological nature to the system [31–33].

While many properties of DSMs have already been explored, there remains a gap in understanding of their optical interactions and topological implications of these interactions. This study aims to address this gap and provide further insights into the optical and topological response of DSM systems [34–50].

In ever-evolving landscape of condensed matter physics, DSMs have emerged as a groundbreaking class of materials captivating scientists with their unique electronic properties and potential applications. These materials are characterized by the presence of Dirac cones in their electronic band structures. This intriguing band structure imparts DSMs with remarkable characteristics such as high mobility of charge carriers, low effective mass, exotic topological states and unusual response to external fields. DSMs stand at the intersection of several fundamental concepts in physics. They exhibit linear dispersion relation near the Fermi level, akin to that observed in two-dimensional graphene. These three-dimensional (3D) analogs of graphene not only expand our understanding of topological phases of matter but also open avenues for practical applications. Indeed, DSMs exhibit a range of unique properties that make them suitable for various cutting-edge applications. Their potential spans multiple advanced technologies, including quantum computing, electronics, spintronics, thermoelectrics, photonics [51, 52].

In this study, we explore the fundamental principles underlying the non-Hermitian aspects of DSMs, focusing on their electronic structure and the role played by the Dirac cones via the non-Hermitian scattering formalism. We examine DSM lasers by means of their associated spectral singularities, review recent developments in characterization of such materials in this context, discuss their theoretical models, and highlight their potential impact on future

technological innovations. By integrating theoretical insights with experimental breakthroughs, this article aims to provide an overview of DSMs and their place in the cutting-edge field of materials science within the context of non-Hermitian physics. In the realm of advanced photonics and materials science, the fusion of DSMs with non-Hermitian physics represents a frontier of unprecedented potential. This innovative intersection promises not only deepens our understanding of quantum materials but also paves the way for revolutionary advancements in laser technology. When subjected to non-Hermitian principles-typically applied to open systems with gain and/or loss-these materials exhibit novel behaviors that are both theoretically intriguing and technologically advantageous.

The non-Hermitian physics explores systems where energy and other observables can exhibit non-conservative dynamics, often due to the presence of gain and/or loss. In such systems, conventional notions of quantum mechanics are modified, leading to novel effects such as exceptional points, unidirectional light propagation, and enhanced lasing performance [54–73]. At exceptional points, although the system may have real eigenvalues, the eigenstates may coalesce. In the case of scattering, the spectral singularities of any optical system in this picture correspond to states of divergent reflection and transmission amplitudes for the real  $k$  values of the physical system [74–82]. This causes the zero-width resonance and the laser threshold state to occur, as it generally produces purely outgoing waves [75]. This is a natural consequence of non-Hermitian physics, unlike traditional lasers. In recent years, very essential studies have been carried out for understanding many unknown aspects of new phenomena and realities with non-Hermitian physics, and numerous studies have recently been devoted to exploring these phenomena [58–70]. Non-Hermitian physics thus plays a crucial role in understanding exotic properties of topological materials [83, 85–87]. This idea constitutes the main motivation of our work. Examining topological systems with non-Hermitian physics is a very interesting and remarkable approach. By integrating DSMs into these non-Hermitian frameworks, researchers are uncovering pathways to engineer lasers with unprecedented efficiency, tunability, and robustness [88, 89].

Given the growing interest in this field and the fact that our topological material of focus has an optically active structure, we will examine how it interacts with electromagnetic waves. Recently, discovery of dichroism effects in DSMs has shown how important it is to study these interactions. Our goal here is to investigate and extract the dichroism effect in these materials. Just as Kerr and Faraday rotations in Weyl semimetals lead to an increase in the system size, dichroism leads to a similar result in a DSM, such that one encounters an additional computational challenge in the structure [83, 84]. However, this challenge also reveals deeper insights into the system. Through our investigations, we uncover previously unknown aspects of DSMs by exploring these complexities. To address this task, we designed our system so that the dichroism effect results in a  $4 \times 4$  transfer matrix, leading to 12 distinct lasing configurations, some of which have topologically robust features. We aim to explore topological effects in our system by generating waves in the TE mode, which will allow us to study the topological characteristics of DSMs. It is well-established that topological properties of DSMs are governed by so-called the  $\theta$  term [32, 90], which is in our case is simply  $\pi$ .

To understand how the  $\theta$  term determines topological properties of DSMs, we analyze scattering behavior of them, identify their spectral singularities, and investigate influence of  $\theta$  term on these singularities. Spectral singularities are the points where continuous spectrum of a system displays exceptional characteristics [74, 91, 92]. Thus, interaction of a DSM with electromagnetic waves can be viewed as a non-Hermitian scattering problem in electromagnetic theory [83].

Our work proceeds as follows. First, we calculate the transfer matrix through boundary conditions by solving Maxwell equations with an axion term specific to DSM for the TE mode configuration. This transfer matrix allows us to calculate the spectral singularities. By calculating the spectral singularities in this way, we determine effect of the  $\theta$  term on the spectral singularities of  $\text{Na}_3\text{Bi}$ , which has been experimentally proven to be a DSM [37, 93–96]. In our investigations, we obtain novel results, such as dichroism in DSMs is an absolute effect and it gives rise to 12 different topological laser types. Accordingly, presence of the  $\theta$  term significantly reduces the gain value in the system. It is manifestly shown that the gain is topologically quantized by degenerating spectral singularity points in the system. This result is very important and has been noticed for the first time. We finally find out that an induced current presents on the surfaces of a DSM. Notable results of this study show that 12 different topological laser types can be created due to the dichroism effect in a DSM, and under what conditions these lasers can exist.

## PRESENCE OF THE $\theta$ TERM AND ELECTRODYNAMICS IN A PLANAR DSM

Before proceeding with the formal derivation, it is useful to briefly clarify the theoretical framework adopted in this work. Our analysis is based on the effective electromagnetic response of Dirac semimetals rather than a microscopic band-Hamiltonian formulation. At low energies, the electronic degrees of freedom in topological semimetals can be integrated out, leading to an effective field theory where the electromagnetic response is governed by Maxwell

equations supplemented by an axion term characterized by the parameter  $\theta$ . This approach, commonly referred to as axion electrodynamics, provides a well-established description of the topological magneto-electric response in Dirac and Weyl semimetals.

Within this effective description, the optical properties of the system can be investigated through the scattering formalism of electromagnetic waves interacting with the material. In such open systems the presence of gain or loss naturally leads to a non-Hermitian framework, where spectral singularities appear as real-frequency poles of the scattering amplitudes. These singularities correspond to zero-width resonances and are known to represent the laser threshold condition in non-Hermitian optical systems. While exceptional points are typically discussed in the context of non-Hermitian Hamiltonians where eigenvalues and eigenvectors coalesce, spectral singularities constitute their scattering-theoretic counterpart. In the present work we therefore focus on the emergence of spectral singularities within the transfer-matrix formulation of the DSM slab system and analyze their physical consequences for the generation of topological laser modes.

Understanding wave propagation in a DSM environment requires grasping the role of  $\theta$  term arising from material properties. The  $\theta$  term is known as the magneto-electric polarizability, and is related to the Berry phase and Chern number. Its mission in electrodynamic interactions is accounted for axion electrodynamics. In Table I, we provide its values in different materials.

TABLE I: The  $\theta$  term for various material types. Here  $b^\mu = (b_0, \vec{b})$ ,  $x^\mu = (t, \vec{x})$ , and the Minkowski metric is assumed to be  $\eta = \text{diag}(-1, +1, +1, +1)$ .

$\theta$	Material Type
0	Ordinary insulators
$\pi$	Time-reversal symmetric topological insulators
$2b_\mu x^\mu$	Weyl semimetals
$\pi$	Dirac semimetals

We consider an optically active linear, homogeneous 3D slab of DSM with thickness  $L$  aligned along the  $z$ -axis as shown in Fig. 1. Although temperature, disorder, and impurities can affect the physical and topological properties of the system, we will simplify our analysis by focusing solely on the effect of the  $\theta$  term. Therefore, we consider a material that is linear, homogeneous, and unaffected by temperature. The  $\theta$  term, which survives both inside and at the boundaries of the DSM, can be expressed as a function of  $z$  in the form  $\theta(z) = \pi \Theta(z) \Theta(L - z)$ , where  $\Theta(z)$  is the Heaviside step function defined as

$$\Theta(z) := \begin{cases} 0, & z < 0 \\ 1, & z \geq 0. \end{cases} \quad (1)$$

This actually demonstrates the semimetallic nature inherent in these materials. Complex refractive index within the slab is considered uniform across the region  $z \in [0, L]$  between its end faces. Observe that the 3D material extends indefinitely in the  $x$  and  $y$  directions. Interaction of this slab system with electromagnetic waves is crucial for understanding its topological and magneto-electric properties, as well as its applications in quantum device technologies. Topological aspects arise from the single placement of Weyl node, which determine the conductive character on the faces of the slab. In our set up, the nodes are located along the  $z$ -axis and a constant  $\theta$  term appears inside the slab.

Maxwell equations incorporating additional topological terms associated with the Weyl node for our slab configuration can be written as [33, 83]

$$\vec{\nabla} \cdot \vec{D}_\ell = \rho, \quad (2)$$

$$\vec{\nabla} \cdot \vec{B}_\ell = 0, \quad (3)$$

$$\vec{\nabla} \times \vec{E}_\ell = -\partial_t \vec{B}_\ell, \quad (4)$$

$$\vec{\nabla} \times \vec{H}_\ell = \vec{J} + \partial_t \vec{D}_\ell. \quad (5)$$

In these equations,  $\vec{D}_\ell$ ,  $\vec{B}_\ell$ ,  $\vec{E}_\ell$  and  $\vec{H}_\ell$  denote linear expressions assumed by the electromagnetic fields in the presence of  $\theta$  term.  $\rho$  and  $\vec{J}$  denote, respectively, the charge and current densities, which depend on position and time. These expressions are free and axion-induced expressions, and can be written as:  $\rho := \rho_f + \rho_\theta$  and  $\vec{J} := \vec{J}_f + \vec{J}_\theta$ . Eqs. (2)-(5)

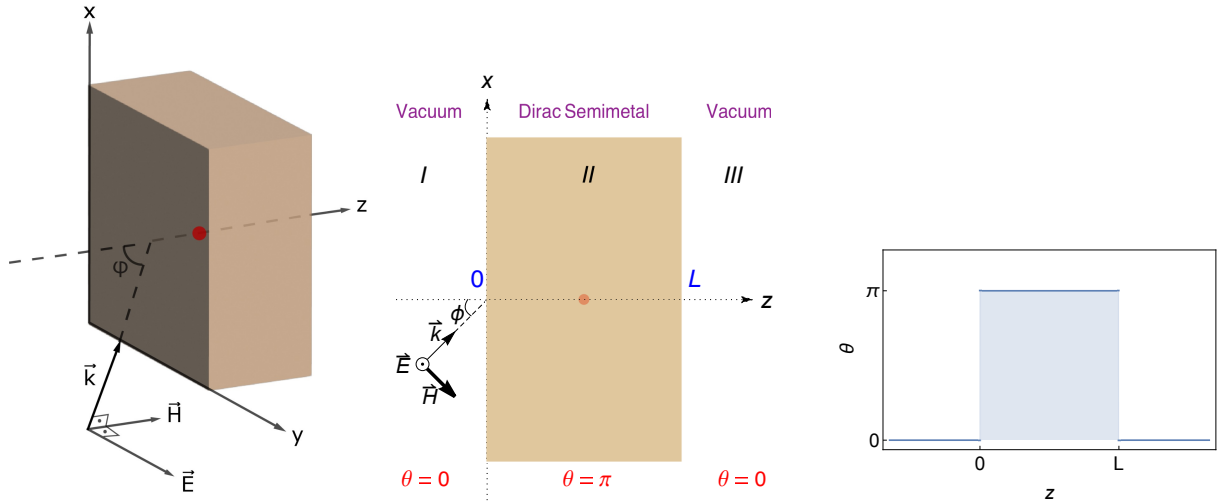


FIG. 1: TE mode configuration for the interaction of electromagnetic wave incident by an angle  $\phi$  measured from the normal to the surface of DSM slab. Left panel displays the 3D configuration while middle panel shows the top view. Red dot identifies the single Weyl node.  $\theta$  terms corresponding to each medium are demonstrated on the right panel. Colored region specifies the DSM.

are Maxwell equations in a DSM environment with a  $\theta$  term. Two different approaches can be followed to obtain these equations. The first of these is to find equations of motion by writing the action expression that specifies interaction between the electromagnetic fields and the  $\theta$  term. The other one is to show interaction of the  $\theta$  term with relevant fields by direct reflection. These are shown in the Appendix.

### Continuity Equation and Axion-Induced Surface Currents

Quantities  $\rho$  and  $\vec{J}$  in Eqs. (2) and (5) satisfy the continuity equation as a natural consequence of Maxwell equations:

$$\vec{\nabla} \cdot \vec{J} + \partial_t \rho = 0 \quad (6)$$

These quantities may be decomposed into free and induced-axion terms, such that two distinct continuity equations are obtained as follows:

$$\vec{\nabla} \cdot \vec{J}_f = 0 \quad (7)$$

$$\vec{\nabla} \cdot \vec{J}_\theta + \partial_t \rho_\theta = 0 \quad (8)$$

Note that here the free charge density is taken as zero. However, due to the semimetallic character of the material, the free current density is different from zero. In this case, divergence of the free current density is zero. The free current density can be related to the conductivity tensor of the material. In this case,

$$\vec{J}_f = \sigma \vec{E}_\ell \quad \Rightarrow \quad [J_f]_\alpha = \sigma_{\alpha\beta} E_\beta. \quad (9)$$

Here  $\sigma$  can be briefly represented as

$$\sigma = \begin{pmatrix} \sigma_{yy} & \sigma_{yz} \\ \sigma_{zy} & \sigma_{zz} \end{pmatrix} \quad (10)$$

It can be seen that  $\sigma_{zz}$  component vanishes due to material properties.

### Scattering Solutions and Dichroism Effect in a Planar Dirac Semimetal

Since the material considered here contains an axionic content, it is inevitable that exotic surface effects will appear when exposed to an external electromagnetic wave. The axionic contribution of the material is considered along the

$z$ -axis only. Thus, if the electromagnetic wave incident from outside has a magnetic field in this direction, a rotation in the polarization direction of the wave is expected. A judicious choice should be made and polarization direction of the electromagnetic wave incident from outside should be sent in a way that it would interact with the axionic term. This corresponds to the TE mode configuration in our study. Hence, a wave polarized along the  $y$ -axis and making an angle of  $\phi$  with the surface normal was sent to the DSM medium from outside, and result of its interaction with the DSM is aimed to be examined within the scope of scattering theory. This choice ensures that the electromagnetic wave couples to the axionic magneto-electric response of the material, which is responsible for the emergence of dichroic behavior. Propagation of the wave in a material is controlled by the solutions of Maxwell equations. Accordingly, by taking the curl (i.e.  $\vec{\nabla} \times$ ) of Eq. (4), and then using Eq. (5), 3D Helmholtz equation is obtained as

$$\nabla^2 \vec{E} + \varepsilon_0 \omega^2 \mathbf{n}^2 \vec{E} + i\omega \mu_0 \vec{J} = 0. \quad (11)$$

Here,  $\mathbf{n}$  represents the complex refractive index of the DSM. For an active material medium with a gain or loss content, the refractive index can be decomposed into its real and imaginary parts as

$$\mathbf{n} = \eta + i\kappa. \quad (12)$$

For various materials, including DSMs, it is in general safe to assume that  $|\kappa| \ll \eta$ , where the parameter  $\kappa$  essentially dictates whether the medium exhibits gain or loss. Specifically, when  $\kappa < 0$ , the medium functions as a gain medium, while for  $\kappa > 0$  the medium behaves as an absorbing or loss medium.

When a wave is incident to the DSM medium from outside with TE mode in  $y$ -direction, some effects will occur when the wave hits the surface due to the electric and magnetic properties of the material. Boundary conditions of the material indicate that the incident wave will not create a (Kerr/Faraday) rotation effect in  $x$ -direction. In this case, it is understood that such types of materials cannot cause a Faraday or Kerr type rotations. However, since the axionic content increases dimension of the electromagnetic wave scattered from the material, the only remaining option is that the polarization direction of the electromagnetic wave in the material will rotate towards the  $z$ -axis. This is known as the dichroism effect and indicates rotation of the wave along the material direction. This effect has actually been observed in such materials, but it is a non-generalized effect that is presented for the first time in this study. The results of this study show that the DSM medium is a dichroic medium. Thus, an electromagnetic wave polarized in the  $y$ -direction will move in the material such a way that it will be polarized in the  $y - z$  plane after the scattering event. In this case, the electric field solution after the scattering can be written as

$$\vec{E}(x, z) = E_y(x, z) \hat{e}_y + E_z(x, z) \hat{e}_z. \quad (13)$$

This expression is inserted into Eq. (11) to obtain the scattering solutions inside and outside of the DSM. It should be noted that current  $\vec{J}$  is zero outside the material. To understand characteristics of these solutions inside the material, values of  $\vec{J}$  are important. As is clearly seen, the free current density that forms  $\vec{J}_f$  exists inside the material due to the dichroism effect. However, induced current  $\vec{J}_\theta$  originating from the axionic term appears only on the surfaces. The reason for this is the presence of Dirac delta functions in the  $\vec{J}_\theta$  expression. In this case, free current densities inside the material can be calculated using Eq. (9). Another point to note is that the dichroism effect only causes existence of the conductivity components  $\sigma_{yz}$  and  $\sigma_{zy}$ . In this case, it can be seen that the Helmholtz equation (11) can be reduced to the following form,

$$\nabla^2 E_\alpha + \varepsilon_0 \omega^2 \mathbf{n}^2 E_\alpha + i\omega \mu_0 \sigma_{\alpha\beta} E_\beta = 0 \quad \Rightarrow \quad [\nabla^2 \delta_{\alpha\beta} + \varepsilon_0 \omega^2 \mathbf{n}^2 \delta_{\alpha\beta} + i\omega \mu_0 \sigma_{\alpha\beta}] E_\beta = 0. \quad (14)$$

Here the subscripts  $\alpha$  and  $\beta$  represent  $y$  and  $z$  components of the electric field. Describing these equations in terms of components yields the following coupled relations:

$$\nabla^2 E_y + \varepsilon_0 \omega^2 \mathbf{n}^2 E_y + i\omega \mu_0 \sigma_{yz} E_z = 0 \quad (15)$$

$$\nabla^2 E_z + \varepsilon_0 \omega^2 \mathbf{n}^2 E_z + i\omega \mu_0 \sigma_{zy} E_y = 0 \quad (16)$$

Note that  $\sigma_{yz} = \sigma_{zy}$  due to the symmetric nature of  $\sigma$ . One can solve these by multiplying Eq. (15) with  $i$ , and then add and subtract it from Eq. (16), yielding the following pair of equations:

$$(\nabla^2 + \varepsilon_0 \omega^2 \mathbf{n}^2) \Phi_\pm \mp \omega \mu_0 \sigma \Phi_\mp = 0. \quad (17)$$

Here,  $\Phi_\pm := E_z \pm iE_y$  and  $\sigma := \sigma_{yz} = \sigma_{zy}$ . Writing this equation explicitly results in coupled new expressions,

$$(\nabla^2 + \varepsilon_0 \omega^2 \mathbf{n}^2) \Phi_+ - \omega \mu_0 \sigma \Phi_- = 0 \quad (18)$$

$$(\nabla^2 + \varepsilon_0 \omega^2 \mathbf{n}^2) \Phi_- + \omega \mu_0 \sigma \Phi_+ = 0 \quad (19)$$

To solve these coupled relations, Eq. (19) is multiplied by  $i$ , then added to and subtracted from Eq. (18). These operations yield the following decoupled equations,

$$(\nabla^2 + \varepsilon_0 \omega^2 \mathbf{n}^2) \Psi_{\pm} \pm i \omega \mu_0 \sigma \Psi_{\pm} = 0, \quad (20)$$

where  $\Psi_{\pm} := \Phi_{+} \pm i \Phi_{-}$ . These solutions in terms of the electric field components can be calculated easily as

$$\Psi_{\pm} := (1 \pm i)(E_z \pm E_y). \quad (21)$$

Thus, components  $E_y$  and  $E_z$  can be calculated in terms of new fields  $\Psi_{+}$  and  $\Psi_{-}$  as

$$E_y = \frac{1}{4} [(1 - i)\Psi_{+} - (1 + i)\Psi_{-}], \quad (22)$$

$$E_z = \frac{1}{4} [(1 - i)\Psi_{+} + (1 + i)\Psi_{-}]. \quad (23)$$

It should be noted that arguments of these quantities depend on  $x$  and  $z$ . As a result, solutions of the decoupled Helmholtz equation (20) can now be easily found. For this purpose, the arguments can be separated as  $\Psi_{\pm}(x, z) = e^{ik_x x} \Psi_{\pm}(z)$ . When these expressions are substituted into Eq. (20), the 1D Helmholtz equation with respect to  $z$  is obtained

$$\Psi_{\pm}''(z) + k_z^2 \tilde{\mathbf{n}}_{\pm}^2 \Psi_{\pm}(z) = 0. \quad (24)$$

In this equation, the prime( $t$ ) symbol indicates the derivative with respect to  $z$ ,  $k_z = k \cos \phi$  is the  $z$ -component of the wave-vector  $\vec{k}$ ,  $\tilde{\mathbf{n}}_{\pm}$  is the frequency dependent birefringence index, which appears due to the conductivity of the material, and it is defined as

$$\tilde{\mathbf{n}}_{\pm} := \sqrt{\tilde{\mathbf{n}}^2 \pm \frac{i \mu_0 \omega \sigma}{k_z^2}}, \quad \tilde{\mathbf{n}} := \frac{\sqrt{\mathbf{n}^2 - \sin^2 \phi}}{\cos \phi}. \quad (25)$$

Notice that Eq. (24) gives rise to the following Schrödinger equation with a constant complex potential  $V_{\pm}(z) := k_z^2(1 - \tilde{\mathbf{n}}_{\pm}^2)$

$$-\Psi_{\pm}''(z) + V_{\pm}(z)\Psi_{\pm}(z) = k_z^2 \Psi_{\pm}(z). \quad (26)$$

As a natural outcome of this analysis, materials exhibiting a DSM phase have two distinct refractive indices (a birefringence effect), with each refractive index corresponding to its own unique Schrödinger equation. This indicates a non-Hermitian state with real energy values, corresponding to the scattering state we described earlier. Here  $\tilde{\mathbf{n}}$  represents the effective refractive index of the material, and is caused by the wave arriving at a certain angle. Thus, solution to the Helmholtz equation, as detailed in Eq. (24), is expressed as follows:

$$\Psi_{\pm}(z) := \begin{cases} A_{1\pm} e^{ik_z z} + B_{1\pm} e^{-ik_z z}, & z < 0 \\ A_{2\pm} e^{ik_z \tilde{\mathbf{n}}_{\pm} z} + B_{2\pm} e^{-ik_z \tilde{\mathbf{n}}_{\pm} z}, & 0 < z < L \\ A_{3\pm} e^{ik_z z} + B_{3\pm} e^{-ik_z z}, & z > L. \end{cases} \quad (27)$$

These results can be substituted into Eqs. (22) and (23) in order to obtain electric field components  $E_y$  and  $E_z$ . Similarly, to find magnetic field  $\vec{B}$ , values of  $E_y$  and  $E_z$  are substituted into Eq. (61). As a result, the field  $\vec{B}(x, z)$  is expressed as:

$$\vec{B} = -\frac{i}{\omega} (\vec{\nabla} \times \vec{E}) = \frac{i}{\omega} [\hat{e}_x \partial_z E_y + \hat{e}_y \partial_x E_z - \hat{e}_z \partial_x E_y]. \quad (28)$$

But since  $E_y(x, z) = e^{ik_x x} \mathcal{E}_y(z)$ , we find

$$\partial_x E_y = ik_x E_y.$$

As a result, these quantities can be made independent of  $x$ , and  $\vec{B}(z)$  is obtained as

$$\vec{B}(z) = \frac{i}{\omega} [\partial_z \mathcal{E}_y \hat{e}_x + ik_x \mathcal{E}_z \hat{e}_y - ik_x \mathcal{E}_y \hat{e}_z]. \quad (29)$$

It will be seen that  $\partial_z \mathcal{E}_y$  is found as follows

$$\partial_z \mathcal{E}_y = \frac{(1-i)}{4} \partial_z \Psi_+ - \frac{(1+i)}{4} \partial_z \Psi_- \quad (30)$$

with

$$\partial_z \Psi_{\pm} := ik_z \tilde{\mathbf{N}}_{\pm} \mathcal{F}_{\pm}^{\pm}, \quad \tilde{\mathbf{N}}_{\pm} := \begin{bmatrix} 1 \\ \tilde{\mathbf{n}}_{\pm} \\ 1 \end{bmatrix}, \quad \mathcal{F}_a^{\ell}(z) := \begin{bmatrix} A_{1a} e^{ik_z z} + \ell B_{1a} e^{-ik_z z} \\ A_{2a} e^{ik_z \tilde{\mathbf{n}}_a z} + \ell B_{2a} e^{-ik_z \tilde{\mathbf{n}}_a z} \\ A_{3a} e^{ik_z z} + \ell B_{3a} e^{-ik_z z} \end{bmatrix}, \quad (31)$$

where the subscripts  $a$  and  $\ell$  take the signs  $+/-$ . Consequently, with these new definitions, the electric and magnetic field components can be determined as in Table II. Likewise, one can obtain the  $\vec{H}$  and  $\vec{D}$  fields using definitions:  $\vec{H} = \vec{B}/\mu_0$  and  $\vec{D} = \varepsilon \vec{E}$ ; their components are given in Table II. Symbol  $\mathbf{N}$ , defined in Table II, represents refractive index of the entire space and is given by:

$$\mathbf{N} := \begin{bmatrix} 1 \\ \mathbf{n} \\ 1 \end{bmatrix} \quad (32)$$

Notice that  $\mathbf{N}$  and  $\tilde{\mathbf{N}}$  can be related to each other by  $\tilde{\mathbf{N}} = \sqrt{\mathbf{N}^2 - \sin^2 \phi} / \cos \phi$ , where  $\tilde{\mathbf{N}}$  represents effective refractive index of the entire space.

TABLE II: Components of the fields  $\vec{\mathbf{Z}} \in \{\vec{E}, \vec{D}, \vec{B}, \vec{H}\}$  inside and outside of the DSM slab. Here  $\vec{\mathbf{Z}}(x, z) := \frac{(1-i)e^{ik_x x}}{4} \vec{\mathcal{Z}}(z)$  and  $\vec{\mathcal{Z}} \in \{\vec{\mathcal{E}}, \vec{\mathcal{D}}, \vec{\mathcal{B}}, \vec{\mathcal{H}}\}$ . Quantities  $\mathcal{F}_a^{\ell}(z)$  are specified in Eq. 31, and the refractive index of whole space is identified in Eq. 32.

$\vec{\mathcal{E}}(z)$	$\vec{\mathcal{D}}(z)$	$\vec{\mathcal{B}}(z)$	$\vec{\mathcal{H}}(z)$
$\mathcal{E}_x = 0$	$\mathcal{D}_x = 0$	$\mathcal{B}_x = -\frac{\cos \phi}{c} [\tilde{\mathbf{N}}_+ \mathcal{F}_+^-(z) - i \tilde{\mathbf{N}}_- \mathcal{F}_-^-(z)]$	$\mathcal{H}_x = -\frac{\cos \phi}{Z_0} [\tilde{\mathbf{N}}_+ \mathcal{F}_+^-(z) - i \tilde{\mathbf{N}}_- \mathcal{F}_-^-(z)]$
$\mathcal{E}_y = [\mathcal{F}_+^+(z) - i \mathcal{F}_-^+(z)]$	$\mathcal{D}_y = \varepsilon_0 \mathbf{N}^2 [\mathcal{F}_+^+(z) - i \mathcal{F}_-^+(z)]$	$\mathcal{B}_y = -\frac{\sin \phi}{c} [\mathcal{F}_+^+(z) + i \mathcal{F}_-^+(z)]$	$\mathcal{H}_y = -\frac{\sin \phi}{Z_0} [\mathcal{F}_+^+(z) + i \mathcal{F}_-^+(z)]$
$\mathcal{E}_z = [\mathcal{F}_+^+(z) + i \mathcal{F}_-^+(z)]$	$\mathcal{D}_z = \varepsilon_0 \mathbf{N}^2 [\mathcal{F}_+^+(z) + i \mathcal{F}_-^+(z)]$	$\mathcal{B}_z = \frac{\sin \phi}{c} [\mathcal{F}_+^+(z) - i \mathcal{F}_-^+(z)]$	$\mathcal{H}_z = \frac{\sin \phi}{Z_0} [\mathcal{F}_+^+(z) - i \mathcal{F}_-^+(z)]$

After determining the electromagnetic fields at every point in space, boundary conditions at the edges of the DSM can be established. Standard boundary conditions for the DSM medium are outlined in Table IV, which is presented in Appendix. Hence, the boundary conditions given in Table IV can be written to relate the amplitudes on the left and right surfaces. Accordingly, the following notations can be used for the fields in regions I - II and II - III, respectively:

$$\mathbb{S} \vec{\mathbf{V}}_2 = \mathbb{U}_+ \vec{\mathbf{V}}_1 \quad \mathbb{S} \mathbb{P}_1 \vec{\mathbf{V}}_2 = \mathbb{U}_- \mathbb{P}_2 \vec{\mathbf{V}}_3 \quad (33)$$

Here we employed the following definitions.

$$\mathbb{U}_{\pm} := \begin{pmatrix} 1 \pm \frac{k_x}{\varepsilon_0 \omega} & 1 \pm \frac{k_x}{\varepsilon_0 \omega} & i(1 \mp \frac{k_x}{\varepsilon_0 \omega}) & i(1 \mp \frac{k_x}{\varepsilon_0 \omega}) \\ 1 & 1 & -i & -i \\ 1 \mp \frac{Z_0 \alpha}{\cos \phi} & -(1 \pm \frac{Z_0 \alpha}{\cos \phi}) & -i(1 \mp \frac{Z_0 \alpha}{\cos \phi}) & i(1 \pm \frac{Z_0 \alpha}{\cos \phi}) \\ 1 \mp \frac{Z_0 \sigma}{\sin \phi} & 1 \mp \frac{Z_0 \sigma}{\sin \phi} & i(1 \mp \frac{Z_0 \sigma}{\sin \phi}) & i(1 \mp \frac{Z_0 \sigma}{\sin \phi}) \end{pmatrix} \quad (34)$$

$$\vec{\mathbf{V}}_i := \begin{bmatrix} A_{i+} \\ B_{i+} \\ A_{i-} \\ B_{i-} \end{bmatrix}, \quad \mathbb{S} := \begin{pmatrix} \mathbf{n}^2 & \mathbf{n}^2 & i \mathbf{n}^2 & i \mathbf{n}^2 \\ 1 & 1 & -i & -i \\ \tilde{\mathbf{n}}_+ & -\tilde{\mathbf{n}}_+ & -i \tilde{\mathbf{n}}_- & i \tilde{\mathbf{n}}_- \\ 1 & 1 & i & i \end{pmatrix} \quad (35)$$

$$\mathbb{P}_1 := \begin{pmatrix} e^{ik_z \tilde{\mathbf{n}}_+ L} & 0 & 0 & 0 \\ 0 & e^{-ik_z \tilde{\mathbf{n}}_+ L} & 0 & 0 \\ 0 & 0 & e^{ik_z \tilde{\mathbf{n}}_- L} & 0 \\ 0 & 0 & 0 & e^{-ik_z \tilde{\mathbf{n}}_- L} \end{pmatrix}, \quad \mathbb{P}_2 := \begin{pmatrix} e^{ik_z L} & 0 & 0 & 0 \\ 0 & e^{-ik_z L} & 0 & 0 \\ 0 & 0 & e^{ik_z L} & 0 \\ 0 & 0 & 0 & e^{-ik_z L} \end{pmatrix} \quad (36)$$

## Transfer Matrix and Spectral Singularities

Transfer matrix can be constructed using the expressions in Eq. (33), which describe relations in the boundary regions of the DSM medium following wave scattering. The resulting transfer matrix for the DSM system is given by

$$\vec{\mathbf{V}}_3 = \mathbf{M}\vec{\mathbf{V}}_1, \quad \mathbf{M} = \mathbb{P}_2^{-1} \mathbf{U}_-^{-1} \mathbb{S} \mathbb{P}_1 \mathbb{S}^{-1} \mathbf{U}_+ \quad (37)$$

Transfer matrix is a very important tool that contains all the basic information in a scattering system, which can be used to control post-scattering behavior of the system. All parameters of the system can be obtained from its transfer matrix. Hence, the exceptional points of DSM environment in the non-Hermitian physics framework can be obtained again through the transfer matrix.

Transfer matrix given by Eq. (37) contains all information about the DSM system; in this section, we obtain its spectral singularities using the transfer matrix. Spectral Singularities in the case of gain doped DSM are associated with exceptional points or non-Hermitian phases where the system exhibits unusual behavior of lasing threshold condition. These correspond to zero-width resonances at real energy eigenstates. As can be understood from our analysis, a 1D DSM becomes 2D system due to the dichroism property even if electromagnetic waves incident in TE mode in 1D. This property causes the transfer matrix to be in the form of a  $4 \times 4$  matrix. Thus, exceptional points in the system can be detected by imposing restrictions on the components of the transfer matrix. As it is known, the exceptional points have bases formed by the state vectors that form the Hilbert space of the system. In a normal Hermitian system, these bases, which should be orthonormal, become parallel to each other and/or their eigenvalues become coincident, resulting in the exceptional points. Since there are 4 orthonormal state vectors originating from two different modes in our system, very different exceptional point configurations can be produced. In this study, only a special case called the spectral singularity is examined. After a scattering event, the spectral singularity in the system forms only wave configurations going outwards. For this, if different solution modes of the system are called plus (+) and minus (−) mode solutions, different spectral singularity situations can be obtained. Each distinct case will be explored separately in the upcoming sections, with realistic DSM examples provided.

We define the gain coefficient of the DSM system as

$$g := -2k\kappa, \quad (38)$$

where  $k = 2\pi/\lambda$  denotes the free-space wavenumber, and  $\kappa$  is the imaginary part of the refractive index  $\mathbf{n}$ , i.e.  $\mathbf{n} = \eta + i\kappa$ . To understand how the physical parameters of our system influence the spectral singularity condition we investigate, as an example, Na<sub>3</sub>Bi in the slab geometry. Na<sub>3</sub>Bi is recognized as one of the first practical DSMs [37, 93–96]. Its characteristics are [51–53]:

$$\eta = 1.33, \quad L = 500 \text{ nm}, \quad \phi = 60^\circ. \quad (39)$$

We notice that refractive index of DSM changes with Fermi energy, ambient temperature, and light frequency [51]. We also require the conductivity of Na<sub>3</sub>Bi for our computational analysis. According to the Kubo formalism, its conductivity in the low temperature limit can be expressed as  $\sigma = \sigma_R + i\sigma_I$  [51, 52, 97, 98], where the real and imaginary parts are approximated as follows:

$$\begin{aligned} \sigma_R &= \frac{e^2}{\hbar} \frac{\mathbf{g}k_F}{24\pi} \Omega \mathbf{G}(\Omega - 2), \\ \sigma_I &= \frac{e^2}{\hbar} \frac{\mathbf{g}k_F}{24\pi} \left[ \frac{4}{\Omega} - \Omega \ln \left( \frac{4\varepsilon_c^2}{|\Omega^2 - 4|} \right) \right], \end{aligned} \quad (40)$$

where  $e$  is the elementary electric charge,  $\mathbf{g}$  indicates the degeneracy factor, and  $\mathbf{G}$  denotes the Riemann–Siegel theta function. The Fermi momentum is given by  $k_F = E_F/(\hbar v_F)$ , where  $\hbar$  is the reduced Planck constant and  $v_F$  is the Fermi velocity of the electrons. Other parameters are defined as  $\Omega = \hbar\omega/E_F + iv_F/E_F k_F \mu$ , where  $\omega$  and  $\mu$  represent the angular frequency of the incident wave and the carrier mobility, respectively, and  $\varepsilon_c = E_c/E_F$ , with  $E_c$  being the cutoff energy. In our case,  $\mathbf{g} = 40$ , Fermi velocity is  $v_F = 10^6$  m/s, Fermi energy level is  $E_F = 0.9$  eV and  $E_c = 3$  eV. We plot the normalized conductivity of Na<sub>3</sub>Bi for these parameters in Fig. 2.

### Plus-Mode Spectral Singularity Configuration: Plus-Mode Topological DSM Laser

In this case, there are only outgoing waves of the Plus Mode on the far right and far left sides of the system (see Fig. 3). Here,  $B_{1+}$  and  $A_{3+}$  are the amplitude of the waves. For this case to happen  $A_{1+} = A_{1-} = B_{1-} = B_{3+} =$

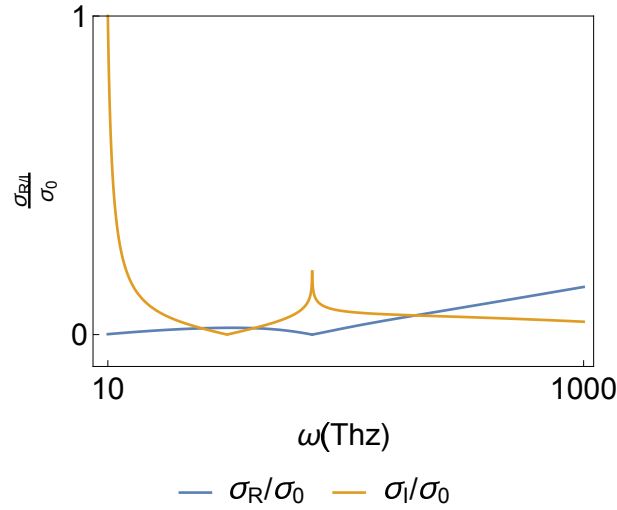


FIG. 2: The frequency-dependent real and imaginary parts of the conductivity for  $\text{Na}_3\text{Bi}$ . The conductivity at 10 THz frequency is indicated by  $\sigma_0$ .

$A_{3-} = B_{3-} = 0$  must be satisfied, which is possible if the condition

$$M_{22} = M_{32} = M_{42} = 0. \quad (41)$$

is satisfied. Here  $M_{i,j}$  are the components of matrix  $M$ . These are the plus-mode spectral singularity conditions.

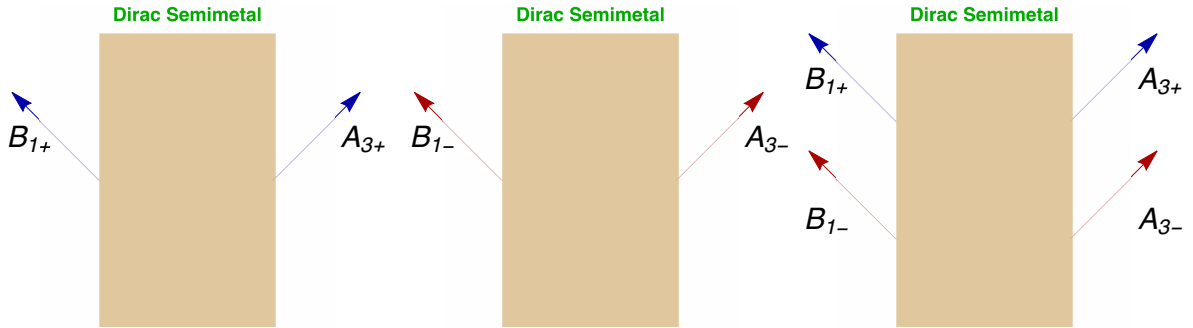


FIG. 3: The spectral singularity configurations and laser output modes of the Plus-Mode (left panel), Minus-Mode (middle panel) and Bimodal case (right panel) in a DSM medium. Waves with amplitudes  $B_{1+}$  and  $A_{3+}$  are output from the left and right sides in the Plus-Mode, amplitudes  $B_{1-}$  and  $A_{3-}$  are for the Minus-Mode, and amplitudes  $B_{1+}$ ,  $B_{1-}$ ,  $A_{3+}$ , and  $A_{3-}$  are for the Bimodal case, respectively.

#### Minus-Mode Spectral Singularity Configuration: Minus-Mode Topological DSM Laser

In this case, the system has only outgoing waves of the Minus-Mode on the far right and far left sides, as shown in Fig. 3. These waves have amplitudes  $B_{1-}$  and  $A_{3-}$ . For this case to occur, we must have  $A_{1+} = A_{1-} = B_{1+} = B_{3+} = A_{3+} = B_{3-} = 0$ . This can only happen if

$$M_{14} = M_{24} = M_{44} = 0 \quad (42)$$

is provided for real  $k$  values. These are the spectral singularity conditions for the Minus-Mode.

### Bimodal Spectral Singularity Configuration: Bimodal Topological DSM Laser

In this case, the system has only outgoing waves of the Bimodal case on the far right and far left sides, as shown in Fig. 3. These waves have amplitudes  $B_{1+}$ ,  $B_{1-}$ ,  $A_{3+}$ , and  $A_{3-}$ . For this to occur, conditions  $A_{1+} = A_{1-} = B_{3+} = B_{3-} = 0$  must be satisfied. This is possible if

$$\mathbb{M}_{22} = \mathbb{M}_{24} = \mathbb{M}_{42} = \mathbb{M}_{44} = 0 \quad (43)$$

is provided for real  $k$ -values. These are the spectral singularity conditions for the Bimodal configuration.

### Random Spectral Singularity Configurations: Random Topological DSM Lasers

The setup we have analyzed enables us to create random spectral singularities, making it possible to generate random laser beam outputs from either side of the DSM, irrespective of any particular lasing mode. This approach illustrates effectiveness of a topological laser configuration for achieving desired outcomes, and demonstrates the potential of our method to yield highly diverse results.

As shown in Table III, 15 different lasing conditions can be achieved in a DSM material. Some of these conditions are appropriate for unidirectional lasing, while others are suitable for bidirectional lasing or random lasing. Achieving a specific lasing configuration requires meeting relevant spectral singularity condition. However, as can be seen in Table III, it is not possible to obtain laser states that only exit from the right side for the wave configurations emitted from the left side. Similarly, for the waves emitted from the right side, only laser configurations that emerge from the left side are not permitted. In this case, the 15 distinct topological laser states observed are actually reduced to 12.

Figure (4) shows components of the transfer matrix. It is manifestly seen which components of the transfer matrix provide the conditions given in Table III, corresponding to distinct laser configurations. Figure (4) reveals that the configurations presented in Table III originate from diverse combinations of components in the second and last columns of the transfer matrix. This highlights that these columns play a pivotal role in determining all distinct laser configurations in a DSM slab.

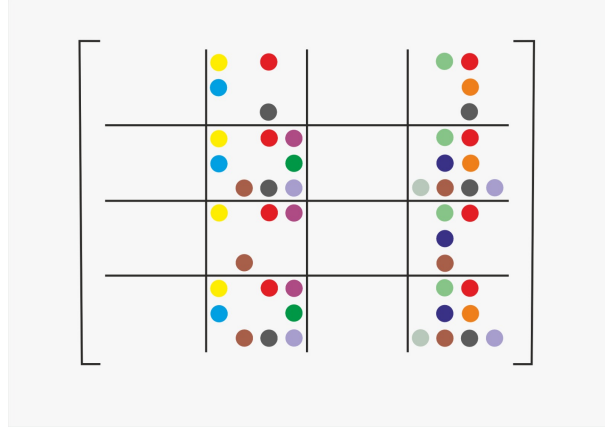


FIG. 4: A diagram of topological DSM laser types within the components of the transfer matrix for a DSM environment. It illustrates the laser generation conditions for each topological DSM laser type listed in Table III, with different colors representing different laser types. Notably, only the second and fourth columns of the transfer matrix generate laser beams.

To understand how a topological DSM laser is shaped based on system parameters, we first need to determine the laser type and apply relevant conditions. Among the 12 laser types, we will focus on only three key ones: Plus-Mode, Minus-Mode, and Bimodal topological DSM lasers. The DSM slab system is influenced by several parameters, such as the gain coefficient  $g$ , wavelength  $\lambda$  of the incoming wave, incident angle  $\phi$ , slab thickness  $L$ , and material type, characterized by  $\eta$ . Desired conditions are determined by optimal interdependence of these parameters. For convenience, we select  $\text{Na}_3\text{Bi}$  as the DSM material, with its properties given in Eq. (39), relationship between  $g$  and  $\lambda$  for three different laser types is shown in Figs. (5), (6), and (7).

TABLE III: All potential laser output configurations and conditions from both sides of the DSM slab for an electromagnetic wave incident from the left side.

Type of Laser	Left Side	Right Side	Spectral Singularity Condition
Unidirectional Laser from Left (+ Mode)	+	None	$M_{12} = M_{22} = M_{32} = M_{42} = 0$
Unidirectional Laser from Left (- Mode)	-	None	$M_{14} = M_{24} = M_{34} = M_{44} = 0$
Unidirectional Laser from Left (Bimodal)	+ & -	None	$M_{12} = M_{22} = M_{32} = M_{42} = 0$ $M_{14} = M_{24} = M_{34} = M_{44} = 0$
Unidirectional Laser from Right (+ Mode)	None	+	NOT allowable
Unidirectional Laser from Right (- Mode)	None	-	NOT allowable
Unidirectional Laser from Right (Bimodal)	None	+ & -	NOT allowable
Bidirectional Laser (+ Mode)	+	+	$M_{22} = M_{32} = M_{42} = 0$
Bidirectional Laser (+ from Left, - from Right)	+	-	$M_{12} = M_{22} = M_{42} = 0$
Bidirectional Laser (- from Left, + from Right)	-	+	$M_{24} = M_{34} = M_{44} = 0$
Bidirectional Laser (- Mode)	-	-	$M_{14} = M_{24} = M_{44} = 0$
Bidirectional Laser (+ from Left, + & - from Right)	+	+ & -	$M_{22} = M_{42} = 0$
Bidirectional Laser (- from Left, + & - from Right)	-	+ & -	$M_{24} = M_{44} = 0$
Bidirectional Laser (+ & - from Left, + from Right)	+ & -	+	$M_{22} = M_{24} = 0$ $M_{32} = M_{34} = 0$ $M_{42} = M_{44} = 0$
Bidirectional Laser (+ & - from Left, - from Right)	+ & -	-	$M_{12} = M_{14} = 0$ $M_{22} = M_{24} = 0$ $M_{42} = M_{44} = 0$
Bidirectional Laser (Bimodal)	+ & -	+ & -	$M_{22} = M_{24} = M_{42} = M_{44} = 0$

Figure 5 presents conditions for the Plus Mode laser type, where only Plus Mode waves can exit from both the right and left sides of the DSM slab. The colored points in panels (a), (b), and (c) represent the spectral singularity points, corresponding to real zeros of  $M_{22}$ ,  $M_{32}$  and  $M_{42}$ , respectively. Black spectral singularity points in panel (d) represent the common values where these zeros occur simultaneously. In other words, the system will lase in Plus-Mode from both sides of the DSM slab at wavelengths indicated by the black points. As shown in panel (d), multiple wavelengths can correspond to the same gain value, or a single wavelength can correspond to multiple gain values. This is a significant result highlighting topological nature of the topological DSM laser. Despite the material having a fixed  $\theta$  value, the behavior of laser remains robust to changes in the system parameters. This demonstrates that the DSM laser is indeed a topological laser.

We observe similar behavior in the Minus-Mode DSM laser shown in Fig. (6). In this case, laser beams are emitted

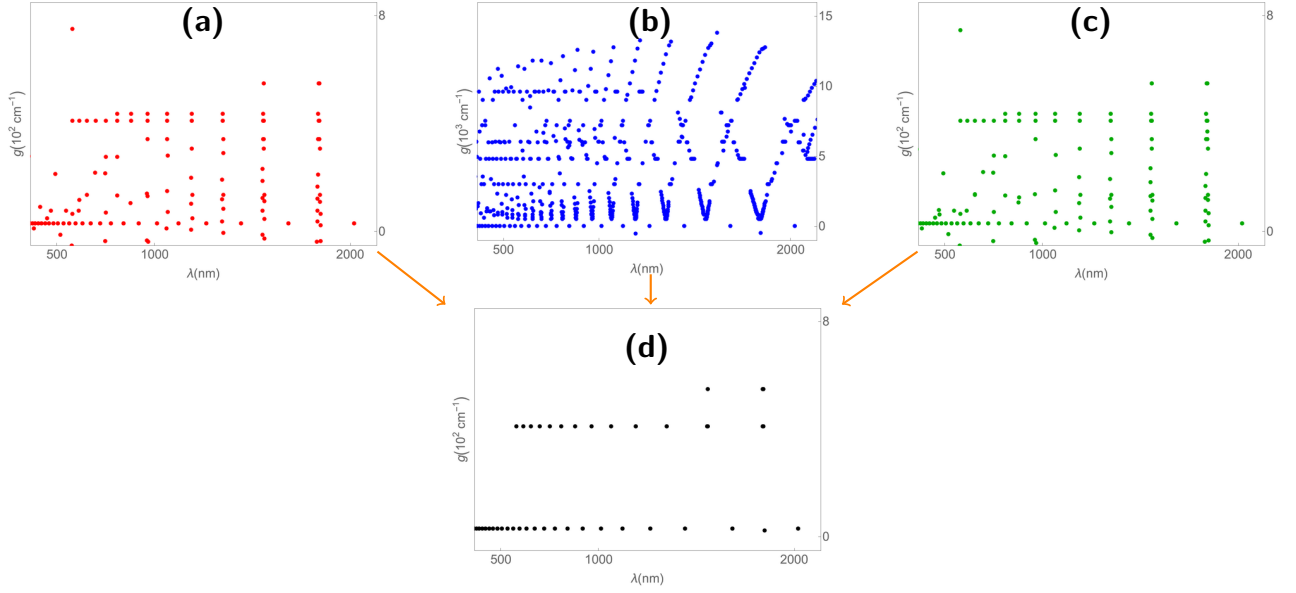


FIG. 5: The spectral singularities are displayed over the  $\lambda - g$  parameters of the Plus Mode configuration. Panels (a), (b) and (c) show the real zero values of components of the transfer matrix separately, while intersection points of these points are shown in panel (d). Graphs are plotted using the data obtained from Eq. (39).

from both sides of the DSM laser. Different colors in the upper part of the figure represent the real zero points of the  $M_{14}$ ,  $M_{24}$  and  $M_{44}$  components of the transfer matrix, respectively. Intersections of these points are marked in black in the lower panel. Additionally, a robust topological laser can be achieved for a wide range of parameter values in the Minus Mode. In this case, the wavelength stability is lower compared to the Plus Mode. However, it is evident that the system can maintain the same gain value across different wavelengths.

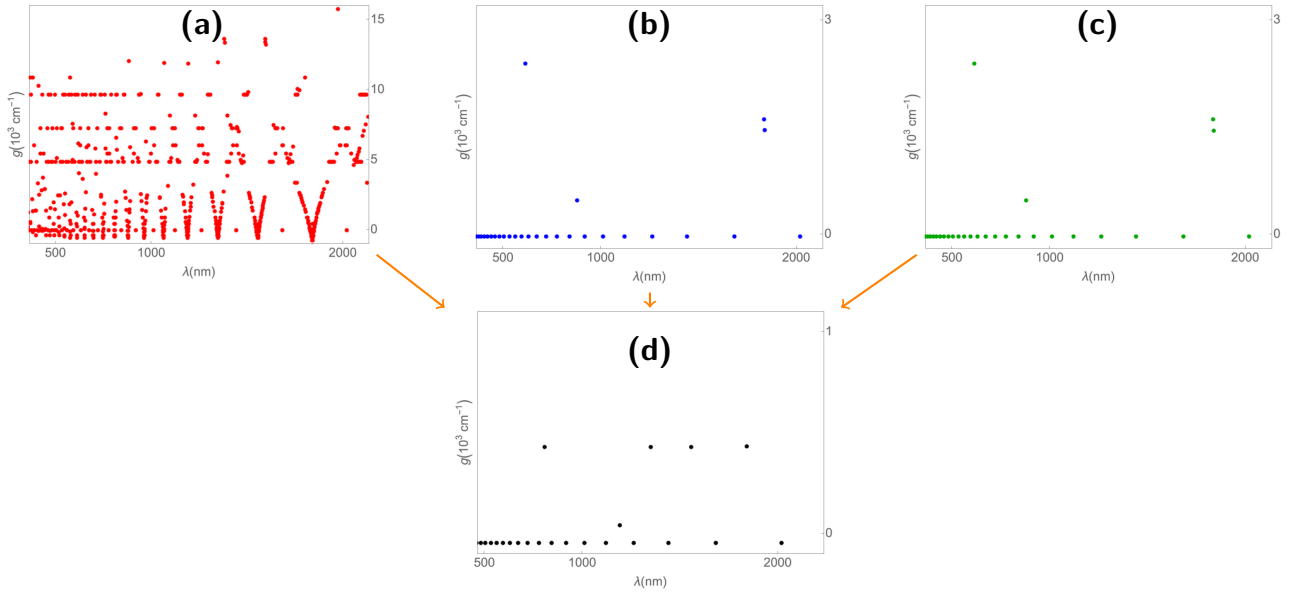


FIG. 6: Spectral singularities as a function of the  $\lambda - g$  parameters in the Minus Mode configuration. Panels (a), (b), and (c) show the real zero values of individual components of the transfer matrix, while intersection points of these zeros are presented in panel (d) below. These graphs are generated using the data provided in Eq. (39).

The final type of DSM laser we will examine is the bimodal configuration, which outputs both Plus and Minus Mode waves from both sides, as shown in Fig. (7). The colored points in the upper panels represent the spectral

singularity points corresponding to the real zeros of the  $M_{22}$ ,  $M_{24}$ ,  $M_{42}$  and  $M_{44}$  components of the transfer matrix. To achieve laser output in both modes from both sides, common intersection points of these spectral singularities must be employed. These intersection points are indicated in black in the lower panel (e). As shown, the system maintains robustness of the gain value, but the gain decreases at the same wavelength. However, the gain remains robust across different wavelengths. We can thus conclude that robustness of the Plus-Mode laser is stronger than that of the Minus and Bimodal configurations. Nevertheless, topological characteristics can be observed in all three cases.

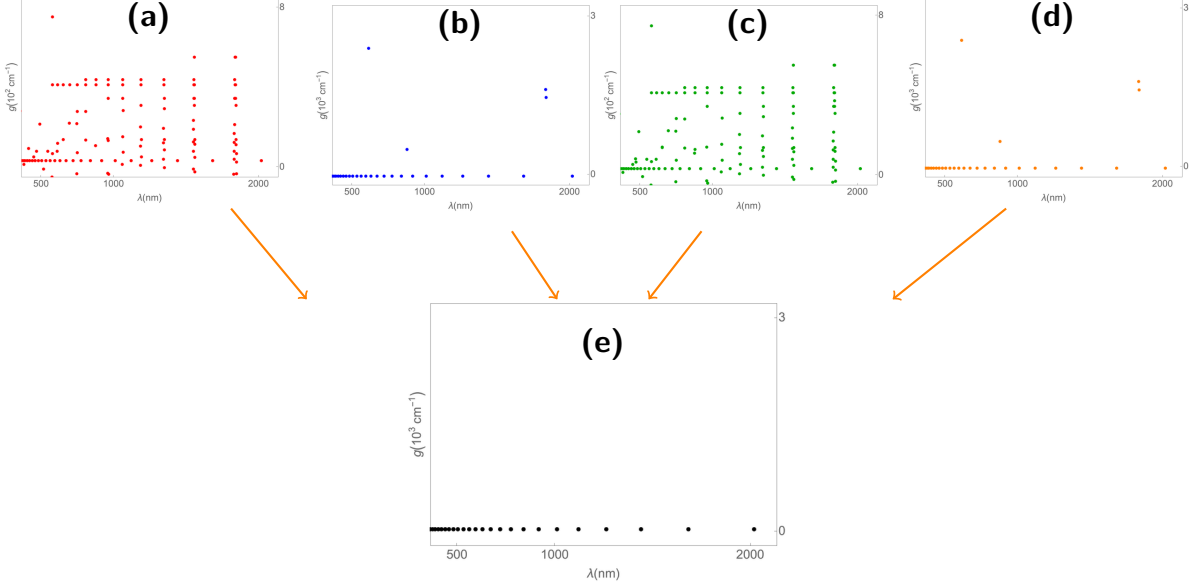


FIG. 7: The spectral singularities as a function of the  $\lambda - g$  parameters for the bimodal configuration. Panels (a), (b), (c), and (d) display the real zero values of individual components of the transfer matrix, while the intersection points of these zeros are shown in panel (e). These graphs are based on the data provided by Eq. (39).

Similar analyses can be conducted for the remaining nine cases to explore interconnected topological characteristics of  $g$  and  $\lambda$ . These analyses may unveil interesting results that have not yet been reported. However, to avoid going off-topic, we will now focus on the effect of another important parameter, incident angle  $\phi$  on the gain value.

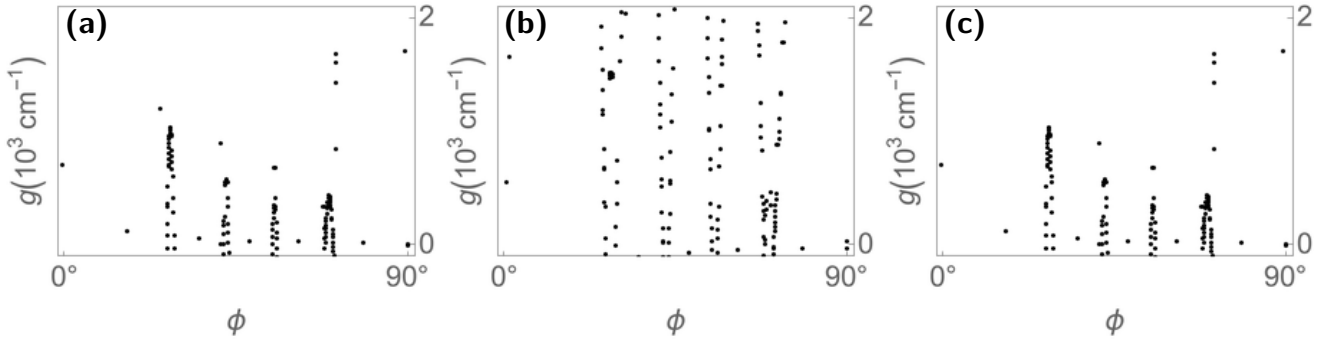


FIG. 8: The spectral singularity points of the Plus Mode [panel (a)], Minus Mode [panel (b)] and Bimodal [panel (c)] cases in the  $\lambda - g$  plane. These points are found by the intersections of points created by the conditions that generate the relevant laser types, as we have shown in Figs. (5), (6) and (7). These graphs are based on the data provided by Eq. (39).

Figure (8) shows how the gain coefficient  $g$  changes with the incident angle  $\phi$  for Plus-Mode, Minus-Mode and Bimodal cases. As can be clearly seen in the figures, it is observed that the gain value and incident angle parameters change in accordance with the topological character of the DSM environment. This is not surprising since this material is topological. The results we found confirm this finding.

It is possible to make similar analysis for other parameters, but we will not discuss them in order to avoid further distraction and because the most important parameters for our system are the gain coefficient, wavelength and incidence angle. All these different configurations occur because the electromagnetic interaction in the DSM medium is dichroic in nature, which is due to the constant axion term that such a medium contains.

### INDUCED SURFACE CURRENT $\vec{J}_\theta$ AND ITS BEHAVIOR AT SPECTRAL SINGULARITIES

Before concluding our discussion, one more important issue needs to be addressed: the axion-induced surface current(s), denoted as  $\vec{J}_\theta$ . Main reason for the formation of this surface current is that, unlike in Weyl semimetals, the  $\theta$ -parameter in DSM undergoes a discontinuous jump at the surface. As demonstrated in Appendix B, the axionic surface current is given by  $\vec{J}_\theta = -\beta\mu\vec{\nabla}\theta \times \vec{E}$ . Using the expression for  $\vec{\nabla}\theta = \pi[\delta(z)\Theta(L-z) + \Theta(z)\delta(L-z)]\hat{e}_k$ , which corresponds to a DSM slab, and the electric field provided in Table II, we can derive the following expression for the axion-induced surface current:

$$\vec{J}_\theta = \frac{(1-i)\beta\mu\pi}{4}[\delta(z)\Theta(L-z) + \Theta(z)\delta(L-z)] [\mathcal{F}_+^+(z) - i\mathcal{F}_-^+(z)] e^{ik_x x} \hat{e}_x. \quad (44)$$

As is evident from this expression, the axion-induced current(s) arise at the surfaces  $z = 0$  and  $z = L$ , and they flow in the  $x$ -direction. To better understand general characteristics of these currents, we will examine three different configurations: the Plus-Mode, Minus-Mode, and Bimodal Cases.

By revisiting the spectral singularity condition for the Plus-Mode, we obtain  $A_{3+} = \mathbb{M}_{12}B_{1+}$ . Thus, it becomes clear that the surface current takes the following simplified form:

$$J_\theta(x, z) := \frac{(1-i)\beta\mu\pi e^{ik_x x} B_{1+}}{4} \begin{cases} 1, & z = 0, \\ \mathbb{M}_{12} e^{ik_z L}, & z = L. \end{cases} \quad (45)$$

Similarly, using the spectral singularity condition for the Minus-Mode, one gets the result  $A_{3-} = \mathbb{M}_{34}B_{1-}$ . Hence, it becomes evident that the surface current simplifies to the following form:

$$J_\theta(x, z) := -\frac{(1+i)\beta\mu\pi e^{ik_x x} B_{1-}}{4} \begin{cases} 1, & z = 0, \\ \mathbb{M}_{34} e^{ik_z L}, & z = L. \end{cases} \quad (46)$$

Finally, by applying the spectral singularity condition for the Bimodal case, we find the expressions  $A_{3+} = \mathbb{M}_{12}B_{1+} + \mathbb{M}_{14}B_{1-}$  and  $A_{3-} = \mathbb{M}_{32}B_{1+} + \mathbb{M}_{34}B_{1-}$ . Therefore, bimodal surface currents at  $z = 0$  and  $z = L$  turn out to be

$$J_\theta(x, z) := \frac{(1-i)\beta\mu\pi e^{ik_x x}}{4} \begin{cases} [B_{1+} - iB_{1-}], & z = 0, \\ [B_{1+}(\mathbb{M}_{12} - i\mathbb{M}_{32}) + B_{1-}(\mathbb{M}_{14} - i\mathbb{M}_{34})] e^{ik_z L}, & z = L. \end{cases} \quad (47)$$

As shown in Fig. (9), surface current configurations induced on the left and right surfaces of the DSM plate are consistent with the expressions derived above. These currents are generated at the spectral singularity points (SSP) within the DSM. These spectral singularity points are SSP1  $\in \{g = 47.166 \text{ cm}^{-1}, \lambda = 1261.75 \text{ nm}, \phi = 60^\circ, L = 5 \mu\text{m}\}$ , SSP2  $\in \{g = 4831.520 \text{ cm}^{-1}, \lambda = 1140.33 \text{ nm}, \phi = 60^\circ, L = 5 \mu\text{m}\}$  and SSP3  $\in \{g = 32.678 \text{ cm}^{-1}, \lambda = 1345.87 \text{ nm}, \phi = 60^\circ, L = 5 \mu\text{m}\}$ , respectively. It should be noted that, apart from the spectral singularity points, a clear phase difference occurs between the left and right surface currents at a different point. However, this phase difference vanishes at the spectral singularity points, as demonstrated in Fig. (9). In addition, current on the right surface is greater than that on the left surface in all three modes.

We know that due to its semimetallic nature, a current  $\vec{J}_f$  flows within a DSM material. However, we will not discuss the details of this current here.

### CONCLUDING REMARKS

The unique properties of semimetallic materials make them particularly fascinating, and their electromagnetic interactions and optical applications have sparked considerable interest. In our study, we aimed to shed light on these intriguing aspects and achieved some very interesting findings. Fundamental characteristics of Dirac and Weyl semimetals arise from the presence of the theta term in their structure. Among these, Dirac semimetals (DSMs) stand

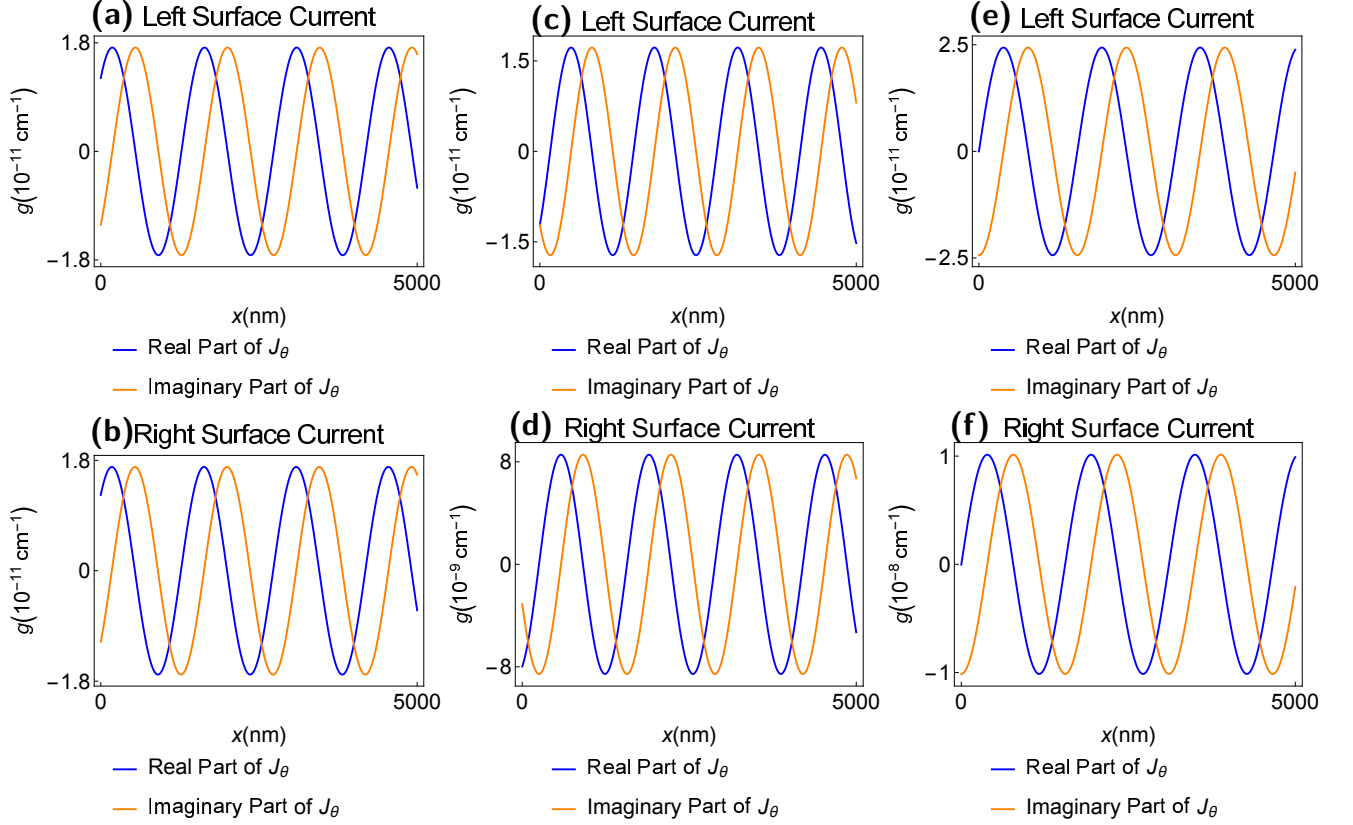


FIG. 9: Current configurations on the left and right surfaces of the DSM slab in three different modes: Plus-Mode, Minus-Mode, and Bimodal Case. Panels (a) and (b) show surface currents in Plus-Mode, panels (c) and (d) depict surface currents in the Minus-Mode, and panels (e) and (f) represent surface currents in the Bimodal Case.

out, as the origin of the theta term lies in the single Dirac cone and a fixed value of the theta parameter. By exploring this distinctive feature from a non-Hermitian perspective, our research led to surprising results that have not been explicitly reported in previous studies. One of the most notable discoveries is that these materials inherently exhibit dichroism, leading to a multidimensional nature in their interactions with electromagnetic waves.

Through our examination of the TE mode solutions, we observed that the dichroism effect exhibited by DSM materials is consistent with experimental findings in the literature, where it has been noted in certain DSM candidate materials. The dichroism effect, as we have shown, also leads to birefringence in these materials. As a consequence, an electromagnetic wave incident on the material for scattering becomes effectively 2D within the material. This alters the transfer matrix, making it  $4 \times 4$  in dimension, which is counter to what one might initially expect. Interestingly, this outcome mirrors a phenomenon we encountered in Weyl semimetals, though it arises from a different cause-Faraday rotation. Despite the similarities, it is important to emphasize that the underlying mechanisms for these effects are fundamentally distinct.

By connecting the scattering solutions of DSMs to non-Hermitian physics and associating them with spectral singularities, we open the door to the possibility of creating a topological laser from these materials. In this study, we explored this potential by investigating how DSMs could serve as the foundation for a topological laser. As is well known, achieving a laser effect requires the presence of spectral singularities, which can be obtained through the transfer matrix. These singularities correspond to the laser threshold conditions that produce zero-width resonance states. Notably, we discovered that DSMs can generate laser output in twelve distinct ways. This phenomenon arises from two different modes present in DSMs-namely, the Plus and Minus Modes-which can each produce different results in a preferred manner. This result, which has not been observed in literature, provides new insight into the behavior of these materials. By examining these different laser modes in detail, we believe we can uncover previously unknown characteristics of DSM materials and open up new possibilities for diverse laser applications.

These materials also give rise to axion-induced surface currents, a phenomenon that holds significant importance for a variety of potential applications. Through our analysis of these currents, we demonstrated that they appear in

phase and in the same direction on both surfaces of the DSM slab. The results of our study, along with the promising application areas, contribute to a deeper understanding of the unique properties of these materials. This insight is likely to generate increased interest and pave the way for a wide range of innovative applications in the near future.

### Appendix A. Derivation of Maxwell Equations and Modified Maxwell Equations in Axion Electrodynamics

In a DSM at low energy limits, a spatially varying axion term plays an important role in determining electromagnetic fields. Total action of the corresponding DSM plate system is defined as the sum of the conventional and axionic terms as follows:  $S = S_0 + S_\theta$ .

$$S_0 = \int \left\{ -\frac{1}{4\mu_0} F_{\mu\nu} F^{\mu\nu} + \frac{1}{2} F_{\mu\nu} \mathcal{P}^{\mu\nu} - J^\mu A_\mu \right\} d^3x dt, \quad (48)$$

$$S_\theta = \frac{\alpha}{8\pi\mu_0} \int \{ \theta(\vec{r}, t) \varepsilon^{\mu\nu\alpha\beta} F_{\mu\nu} F_{\alpha\beta} \} d^3x dt, \quad (49)$$

Here,  $\mathcal{P}^{\mu\nu}$  represents the electric polarization and magnetization given by  $\mathcal{P}^{0i} = cP^i$  and  $\mathcal{P}^{ij} = -\varepsilon^{ijk} M_k$ , respectively.  $A_\mu$  is the 4-vector potential, and  $F_{\mu\nu}$  is the completely antisymmetric electromagnetic field strength tensor. The axion term, which depends on space and time, is given by  $\theta(\vec{r}, t) = \pi \Theta(z) \Theta(L-z)$ , where  $\Theta(z)$  is the Heaviside step function. For a DSM, the  $\theta$  term is time-independent and takes a constant value of  $\pi$  within a limited region. Taking variation of the action with respect to  $A_\mu$ , following equations of motion are obtained.

$$-\frac{1}{\mu_0} \partial_\nu F^{\mu\nu} + \partial_\nu \mathcal{P}^{\mu\nu} + \frac{\alpha}{2\pi\mu_0} \varepsilon^{\mu\nu\alpha\beta} \partial_\nu (\Theta F_{\alpha\beta}) = J^\mu \quad (50)$$

Writing this equation yields modified Maxwell equations given in Eqs. (2), (3), (4), and (5) in the presence of the axion field.

### B. Modified Maxwell Equations in Axion Electrodynamics

Similarly, Maxwell equations can also be derived using a different method. To do this, first note that in classical electromagnetic theory, the fields  $\vec{D}$  and  $\vec{H}$  are written as

$$\vec{D} = \epsilon \vec{E} + \vec{P} \quad (51)$$

$$\vec{H} = \vec{B}/\mu - \vec{M}. \quad (52)$$

The expressions for  $\vec{M}$  and  $\vec{P}$  are derived from the Helmholtz free energy:  $\vec{M} = -\partial \vec{F} / \partial \vec{B}$  and  $\vec{P} = -\partial \vec{F} / \partial \vec{E}$ ,

$$\vec{D} = \epsilon \vec{E} - \beta \theta \vec{B} \quad (53)$$

$$\vec{H} = \vec{B}/\mu + \beta \theta \vec{E} \quad (54)$$

Here,  $\epsilon$  is the dielectric tensor,  $\mu$  is the magnetic permeability coefficient, and  $\beta := 2\alpha/\pi Z_0$ , with  $\alpha := e^2/4\pi\epsilon_0\hbar c$  is the fine structure constant,  $Z_0 := \sqrt{\mu_0/\epsilon_0}$  is the vacuum impedance,  $e$  is the electron charge, and  $c := 1/\sqrt{\epsilon_0\mu_0}$  is the speed of light in vacuum. Hence, Maxwell equations change as follows:

$$\vec{\nabla} \cdot (\epsilon \vec{E} - \beta \theta \vec{B}) = \rho_f \Rightarrow \vec{\nabla} \cdot (\epsilon \vec{E}) = (\rho_f + \rho_\theta) \quad (55)$$

Here,  $\rho_\theta = \beta \vec{\nabla} \theta \cdot \vec{B}$  is the axionic charge density. From Eq. (52), following relations are obtained:

$$\vec{\nabla} \times (\vec{B}/\mu + \beta \theta \vec{E}) = \vec{J}_f + \frac{\partial}{\partial t} (\epsilon \vec{E} - \beta \theta \vec{B}) \quad (56)$$

$$\vec{\nabla} \times \vec{B} = \mu \vec{J}_f + \epsilon \mu \frac{\partial \vec{E}}{\partial t} + \vec{J}_\theta, \quad (57)$$

where,  $\vec{J}_\theta = -\beta\mu(\dot{\theta}\vec{B} + \vec{\nabla}\theta \times \vec{E})$  is the current density due to the axion field (axion-induced current density). For a Dirac half-metal with boundaries at 0 and  $L$ ,  $\vec{\nabla}\theta = \pi[\delta(z)\Theta(L-z) + \Theta(z)\delta(L-z)]$  and  $\dot{\theta} = 0$ . Using  $\vec{H}_\ell = \frac{\vec{B}_\ell}{\mu}$ , Eqs. (55) and (56) become:

$$\vec{\nabla} \cdot \vec{D}_\ell = \rho_f + \rho_\theta \quad (58)$$

$$\vec{\nabla} \times \vec{H}_\ell = \partial_t \vec{D}_\ell + \vec{J}_f + \vec{J}_\theta \quad (59)$$

The other two Maxwell equations remain unchanged:

$$\vec{\nabla} \cdot \vec{B}_\ell = 0 \quad (60)$$

$$\vec{\nabla} \times \vec{E}_\ell + \partial_t \vec{B}_\ell = 0 \quad (61)$$

These equations are Maxwell equations in the presence of the axion term, which we have been used in our calculations. In this study, in order to distinguish between the field values with and without the axion term, the subscript  $\ell$  has been used in the fields when the axion is present. This letter signifies a linear field in the presence of the axion.

### C. Standard Boundary Conditions for a DSM Medium

Once electromagnetic fields at each point in space are determined, boundary conditions at the boundaries of the DSM medium can also be found. To do this, a surface  $S$  is imagined that divides space into two separate regions. Standard boundary conditions for this surface are expressed as follows:

- 1) Tangential component of the electric field  $\vec{E}$  at the interface is continuous:  $\hat{n} \times (\vec{E}_1 - \vec{E}_2) = 0$ .
- 2) Normal component of the magnetic field  $\vec{B}$  perpendicular to the surface must be continuous:  $\hat{n} \cdot (\vec{B}_1 - \vec{B}_2) = 0$ .
- 3) Component of the electric flux density vector  $\vec{D}$  normal to the surface exhibits a ‘‘discontinuity’’ that depends on the surface charge density:  $\hat{n} \cdot (\vec{D}_1 - \vec{D}_2) = \rho^s$ .
- 4) Tangential component of the  $\vec{H}$  field to the surface exhibits a ‘‘discontinuity’’ equivalent to the surface current density:  $\hat{n} \times (\vec{H}_1 - \vec{H}_2) = \vec{J}^s$ .

Definition of  $\hat{n}$  in the boundary conditions specified here represents the unit normal vector of the surface  $S$  directed from region ‘2’ to region ‘1’.  $\rho^s$  and  $\vec{J}^s$  denote the surface charge and current densities, respectively. Standard boundary conditions for the DSM medium are obtained as shown in Table IV:

### ACKNOWLEDGEMENT

This work is funded by Scientific Research Projects Coordination Unit (BAP) of Istanbul University Project Number FBA-2020-35018.

**Competing Interests:** The authors declare no competing interests.

**Data Availability Statement:** The authors declare that any data that support the findings of this study are included within the article.

TABLE IV: Boundary conditions for a DSM of the wave configuration employed in TE mode, where  $\tilde{n}_\pm$ 's are the effective birefringence indices.

---



---


$$\mathbf{n}^2 [(A_{2+} + B_{2+}) + i(A_{2-} + B_{2-})] = \left(1 + \frac{k_x}{\varepsilon_0\omega}\right) (A_{1+} + B_{1+}) + i \left(1 - \frac{k_x}{\varepsilon_0\omega}\right) (A_{1-} + B_{1-})$$


---


$$\left(1 - \frac{Z_0\alpha}{\cos\theta}\right) [A_{1+} - iA_{1-}] - \left(1 + \frac{Z_0\alpha}{\cos\theta}\right) [B_{1+} - iB_{1-}] = \tilde{\mathbf{n}}_+ (A_{2+} - B_{2+}) - i\tilde{\mathbf{n}}_- (A_{2-} - B_{2-})$$


---


$$(A_{2+} + B_{2+}) - i(A_{2-} + B_{2-}) = (A_{1+} + B_{1+}) - i(A_{1-} + B_{1-})$$


---


$$(A_{2+} + B_{2+}) + i(A_{2-} + B_{2-}) = \left(1 - \frac{Z_0\sigma}{\sin\theta}\right) [(A_{1+} + B_{1+}) + i(A_{1-} + B_{1-})]$$


---


$$\mathbf{n}^2 \left[ (A_{2+}e^{ik_z\tilde{\mathbf{n}}_+L} + B_{2+}e^{-ik_z\tilde{\mathbf{n}}_+L}) + i(A_{2-}e^{ik_z\tilde{\mathbf{n}}_-L} + B_{2-}e^{-ik_z\tilde{\mathbf{n}}_-L}) \right]$$

$$= \left(1 - \frac{k_x}{\varepsilon_0\omega}\right) (A_{3+}e^{ik_zL} + B_{3+}e^{-ik_zL}) + i \left(1 + \frac{k_x}{\varepsilon_0\omega}\right) (A_{3-}e^{ik_zL} + B_{3-}e^{-ik_zL})$$


---


$$\tilde{\mathbf{n}}_+ [A_{2+}e^{ik_z\tilde{\mathbf{n}}_+L} - B_{2+}e^{-ik_z\tilde{\mathbf{n}}_+L}] - i\tilde{\mathbf{n}}_- [A_{2-}e^{ik_z\tilde{\mathbf{n}}_-L} - B_{2-}e^{-ik_z\tilde{\mathbf{n}}_-L}]$$

$$= \left(1 + \frac{Z_0\alpha}{\cos\theta}\right) [A_{3+} - iA_{3-}]e^{ik_zL} - \left(1 - \frac{Z_0\alpha}{\cos\theta}\right) [B_{3+} - iB_{3-}]e^{-ik_zL}$$


---


$$(A_{2+}e^{ik_z\tilde{\mathbf{n}}_+L} + B_{2+}e^{-ik_z\tilde{\mathbf{n}}_+L}) - i(A_{2-}e^{ik_z\tilde{\mathbf{n}}_-L} + B_{2-}e^{-ik_z\tilde{\mathbf{n}}_-L}) = (A_{3+} - iA_{3-})e^{ik_zL} + (B_{3+} - iB_{3-})e^{-ik_zL}$$


---


$$[A_{2+}e^{ik_z\tilde{\mathbf{n}}_+L} + B_{2+}e^{-ik_z\tilde{\mathbf{n}}_+L}] + i[A_{2-}e^{ik_z\tilde{\mathbf{n}}_-L} - B_{2-}e^{-ik_z\tilde{\mathbf{n}}_-L}]$$

$$= \left(1 + \frac{Z_0\sigma}{\sin\theta}\right) [(A_{3+} + iA_{3-})e^{ik_zL} + (B_{3+} + iB_{3-})e^{-ik_zL}]$$


---



---

\* mustafa.sarisaman@istanbul.edu.tr

† murat.tas@gtu.edu.tr

‡ taleskirca@gmail.com

- [1] Nash, C. (1999). Topology and physics—a historical essay. *History of topology*, 359-415.
- [2] Simon, David S. Simon. (2018). *Topology and physics: a historical overview*, Tying Light in Knots, Morgan and Claypool Publishers, 2053-2571, 1-7.
- [3] Moessner, Roderich, and Joel E. Moore. *Topological phases of matter*. Cambridge University Press, (2021).
- [4] Wen, X. G. (2017). Colloquium: Zoo of quantum-topological phases of matter. *Reviews of Modern Physics*, 89(4), 041004.
- [5] Witten, E. (2016). Three lectures on topological phases of matter. *La Rivista del Nuovo Cimento*, 39, 313-370.
- [6] Yan, B., and Zhang, S. C. (2012). Topological materials. *Reports on Progress in Physics*, 75(9), 096501.
- [7] Vergniory, M. G., Elcoro, L., Felser, C., Regnault, N., Bernevig, B. A., and Wang, Z. (2019). A complete catalogue of high-quality topological materials. *Nature*, 566(7745), 480-485.
- [8] Yan, B., and Felser, C. (2017). Topological materials: Weyl semimetals. *Annual Review of Condensed Matter Physics*, 8, 337-354.
- [9] Zhang, T., Jiang, Y., Song, Z., Huang, H., He, Y., Fang, Z., ... and Fang, C. (2019). Catalogue of topological electronic materials. *Nature*, 566(7745), 475-479.
- [10] Wieder, Benjamin J., et al. "Topological materials discovery from crystal symmetry." *Nature Reviews Materials* 7.3 (2022): 196-216.
- [11] Ando, Y. (2013). Topological insulator materials. *Journal of the Physical Society of Japan*, 82(10), 102001.
- [12] He, K., Wang, Y., and Xue, Q. K. (2018). Topological materials: quantum anomalous Hall system. *Annual Review of Condensed Matter Physics*, 9, 329-344.
- [13] Hasan, M. Z., and Kane, C. L. (2010). Colloquium: topological insulators. *Reviews of modern physics*, 82(4), 3045.

- [14] Franz, M., and Molenkamp, L. (2013). Topological insulators. Elsevier.
- [15] Bernevig, Andrei, et al. "Recent progress in the study of topological semimetals." *Journal of the Physical Society of Japan* 87.4 (2018): 041001.
- [16] Gao, H., Venderbos, J. W., Kim, Y., and Rappe, A. M. (2019). Topological semimetals from first principles. *Annual Review of Materials Research*, 49, 153-183.
- [17] Weng, H., Dai, X., and Fang, Z. (2016). Topological semimetals predicted from first-principles calculations. *Journal of Physics: Condensed Matter*, 28(30), 303001.
- [18] Yang, Y. B., Qin, T., Deng, D. L., Duan, L. M., and Xu, Y. (2019). Topological amorphous metals. *Physical review letters*, 123(7), 076401.
- [19] Young, Steve M., et al. "Dirac semimetal in three dimensions." *Physical review letters* 108.14 (2012): 140405.
- [20] Liu, Z. K., et al. "Discovery of a three-dimensional topological Dirac semimetal, Na<sub>3</sub>Bi." *Science* 343.6173 (2014): 864-867.
- [21] Borisenko, Sergey, et al. "Experimental realization of a three-dimensional Dirac semimetal." *Physical review letters* 113.2 (2014): 027603.
- [22] Armitage, N. P., E. J. Mele, and Ashvin Vishwanath. "Weyl and Dirac semimetals in three-dimensional solids." *Reviews of Modern Physics* 90.1 (2018): 015001.
- [23] Crassee, I., et al. "3D Dirac semimetal Cd<sub>3</sub>As<sub>2</sub>: A review of material properties." *Physical Review Materials* 2.12 (2018): 120302.
- [24] Young, Steve M., and Charles L. Kane. "Dirac semimetals in two dimensions." *Physical review letters* 115.12 (2015): 126803.
- [25] Wang, Zhijun, et al. "Three-dimensional Dirac semimetal and quantum transport in Cd<sub>3</sub>As<sub>2</sub>." *Physical Review B—Condensed Matter and Materials Physics* 88.12 (2013): 125427.
- [26] Liu, Z. K., et al. "A stable three-dimensional topological Dirac semimetal Cd<sub>3</sub>As<sub>2</sub>." *Nature materials* 13.7 (2014): 677-681.
- [27] Zheng, Guolin, et al. "Transport evidence for the three-dimensional Dirac semimetal phase in ZrTe<sub>5</sub>." *Physical Review B* 93.11 (2016): 115414.
- [28] Gibson, Q. D., et al. "Three-dimensional Dirac semimetals: Design principles and predictions of new materials." *Physical Review B* 91.20 (2015): 205128.
- [29] Neupane, Madhab, et al. "Observation of a three-dimensional topological Dirac semimetal phase in high-mobility Cd<sub>3</sub>As<sub>2</sub>." *Nature communications* 5.1 (2014): 3786.
- [30] Yi, Hemian, et al. "Evidence of topological surface state in three-dimensional Dirac semimetal Cd<sub>3</sub>As<sub>2</sub>." *Scientific Reports* 4.1 (2014): 6106.
- [31] Wilczek, Frank. "Two applications of axion electrodynamics." *Physical review letters* 58.18 (1987): 1799.
- [32] Sekine, Akihiko, and Kentaro Nomura. "Axion electrodynamics in topological materials." *Journal of Applied Physics* 129.14 (2021).
- [33] M. Kargarian, M. Randeria, and N. Trivedi, *Scientific Reports* **5**, 12683 (2015).
- [34] Ma, Qiong, et al. "Direct optical detection of Weyl fermion chirality in a topological semimetal." *Nature Physics* 13.9 (2017): 842-847.
- [35] Tabert, C. J., J. P. Carbotte, and E. J. Nicol. "Optical and transport properties in three-dimensional Dirac and Weyl semimetals." *Physical Review B* 93.8 (2016): 085426.
- [36] Ooi, Kelvin JA, et al. "Nonlinear plasmonics of three-dimensional Dirac semimetals." *Apl Photonics* 4.3 (2019).
- [37] Dadsetani, Mehrdad, and Ali Ebrahimian. "Optical distinctions between Weyl semimetal TaAs and Dirac semimetal Na<sub>3</sub>Bi: An ab initio investigation." *Journal of Electronic Materials* 45 (2016): 5867-5876.
- [38] Meng, Haiyu, et al. "Terahertz polarization conversion from optical dichroism in a topological Dirac semimetal." *Applied Physics Letters* 121.19 (2022).
- [39] Sharafeev, A., et al. "Optical phonon dynamics and electronic fluctuations in the Dirac semimetal Cd<sub>3</sub>As<sub>2</sub>." *Physical Review B* 95.23 (2017): 235148.
- [40] Bafekry, A., et al. "A Dirac-semimetal two-dimensional BeN<sub>4</sub>: Thickness-dependent electronic and optical properties." *Applied Physics Letters* 118.20 (2021).
- [41] Neubauer, David, et al. "Interband optical conductivity of the [001]-oriented Dirac semimetal Cd<sub>3</sub>As<sub>2</sub>." *Physical Review B* 93.12 (2016): 121202.
- [42] Chen, R. Y., et al. "Optical spectroscopy study of the three-dimensional Dirac semimetal ZrTe<sub>5</sub>." *Physical Review B* 92.7 (2015): 075107.
- [43] Lim, J., et al. "Broadband strong optical dichroism in topological Dirac semimetals with Fermi velocity anisotropy." *Chinese Physics B* 29.7 (2020): 077802.
- [44] Shi, Li-kun, and Justin CW Song. "Large optical conductivity of Dirac semimetal Fermi arc surface states." *Physical Review B* 96.8 (2017): 081410.
- [45] Mosca Conte, Adriano, Olivia Pulci, and Friedhelm Bechstedt. "Electronic and optical properties of topological semimetal Cd<sub>3</sub>As<sub>2</sub>." *Scientific Reports* 7.1 (2017): 45500.
- [46] Crassee, I., et al. "3D Dirac semimetal Cd<sub>3</sub>As<sub>2</sub>: A review of material properties." *Physical Review Materials* 2.12 (2018): 120302.
- [47] Kupčić, Ivan, and Josip Kordić. "Optical conductivity of anisotropic Dirac semimetals: The relaxation-time approximation." *Physical Review B* 109.4 (2024): 045426.
- [48] Duan, Wenye, XiangDong Lu, and Jun-Feng Liu. "Large optical conductivity of Fermi arc states in Weyl and Dirac semimetal nanowires." *Physical Review B* 108.19 (2023): 195436.

- [49] Neubauer, David. "Optical and magneto-optical investigations on 3D Dirac-and Weyl-semimetals." (2017).
- [50] Kupčić, I., and J. Kordić. "Optical properties of anisotropic Dirac semimetals." arXiv preprint arXiv:2310.10172 (2023).
- [51] Ye, Yunyang, et al. "Tunable mid-infrared refractive index sensor with high angular sensitivity and ultra-high figure-of-merit based on Dirac semimetal." *Results in Physics* 17 (2020): 103035.
- [52] Zheng, Qiwen, et al. "Theoretical model for a highly sensitive near infrared biosensor based on Bloch surface wave with Dirac semimetal." *Biosensors* 11.10 (2021): 390.
- [53] W. T. Silfvast, *Laser Fundamentals*, Cambridge University Press, Cambridge, 1996.
- [54] C. M. Bender and S. Boettcher, *Phys. Rev. Lett.* **80**, 5243 (1998); K. G. Makris, R. El-Ganainy, D. N. Christodoulides, and Z. H. Musslimani, *Phys. Rev. Lett.* **100**, 103904 (2008).
- [55] A. Mostafazadeh, *Int. J. Geom. Meth. Mod. Phys.* **7**, 1191 (2010); C. M. Bender, D. C. Brody, and H. F. Jones, *Am. J. Phys.* **71**, 1095 (2003).
- [56] S. Longhi, *Phys. Rev. A* **82**, 032111 (2010).
- [57] S. Longhi, *J. Phys. A* **44**, 485302 (2011).
- [58] Ashida, Yuto, Zongping Gong, and Masahito Ueda. "Non-hermitian physics." *Advances in Physics* 69.3 (2020): 249-435.
- [59] Kawabata, Kohei, et al. "Symmetry and topology in non-Hermitian physics." *Physical Review X* 9.4 (2019): 041015.
- [60] El-Ganainy, Ramy, et al. "Non-Hermitian physics and PT symmetry." *Nature Physics* 14.1 (2018): 11-19.
- [61] Okuma, Nobuyuki, and Masatoshi Sato. "Non-Hermitian topological phenomena: A review." *Annual Review of Condensed Matter Physics* 14 (2023): 83-107.
- [62] Wang, Hongfei, et al. "Topological physics of non-Hermitian optics and photonics: a review." *Journal of Optics* 23.12 (2021): 123001.
- [63] Bergholtz, Emil J., Jan Carl Budich, and Flore K. Kunst. "Exceptional topology of non-Hermitian systems." *Reviews of Modern Physics* 93.1 (2021): 015005.
- [64] Bender, Carl M. "Making sense of non-Hermitian Hamiltonians." *Reports on Progress in Physics* 70.6 (2007): 947.
- [65] Bandres, Miguel A., and Mordechai Segev. "Non-Hermitian topological systems." *Physics* 11 (2018): 96.
- [66] Ding, Kun, Chen Fang, and Guancong Ma. "Non-Hermitian topology and exceptional-point geometries." *Nature Reviews Physics* 4.12 (2022): 745-760.
- [67] Moiseyev, Nimrod. *Non-Hermitian quantum mechanics*. Cambridge University Press, 2011.
- [68] Ghatak, Ananya, and Tanmoy Das. "New topological invariants in non-Hermitian systems." *Journal of Physics: Condensed Matter* 31.26 (2019): 263001.
- [69] Martinez Alvarez, V. M., et al. "Topological states of non-Hermitian systems." *The European Physical Journal Special Topics* 227 (2018): 1295-1308.
- [70] Gong, Zongping, et al. "Topological phases of non-Hermitian systems." *Physical Review X* 8.3 (2018): 031079.
- [71] Sarisaman, Mustafa, et al. "Energy Stored in a Slab Covered by Graphene Sheets." *Carbon Related Materials: Commemoration for Nobel Laureate Professor Suzuki Special Symposium at IUMRS-ICAM2017*. Springer Singapore, 2021.
- [72] Mandal, Ipsita, and Emil J. Bergholtz. "Symmetry and higher-order exceptional points." *Physical review letters* 127.18 (2021): 186601.
- [73] Yang, Kang, and Ipsita Mandal. "Enhanced eigenvector sensitivity and algebraic classification of sublattice-symmetric exceptional points." *Physical Review B* 107.14 (2023): 144304.
- [74] A. Mostafazadeh, *Geometric Methods in Physics, Trends in Mathematics*, edited by P. Kielanowski, P. Bieliavsky, A. Odziejewicz, M. Schlichenmaier, and T. Voronov (Springer, Cham, 2015) pp 145-165; arXiv: 1412.0454.
- [75] A. Mostafazadeh, *Phys. Rev. Lett.* **102**, 220402 (2009).
- [76] A. Mostafazadeh, M. Sarisaman, *Phys. Lett. A* **375**, 3387 (2011); *Proc. R. Soc. Lond. Ser. A Math. Phys. Eng. Sci.* **468**, 3224 (2012); *Phys. Rev. A* **87**, 063834 (2013); *Phys. Rev. A* **88**, 033810 (2013); *Phys. Rev. A* **91**, 043804 (2015).
- [77] A. Mostafazadeh and M. Sarisaman, *Ann. Phys. (NY)* **375**, 265-287 (2016).
- [78] A. Mostafazadeh, *Phys. Rev. A* **83**, 045801 (2011).
- [79] A. Mostafazadeh, *Phys. Rev. A* **87**, 012103 (2012).
- [80] Ramezani, Hamidreza, et al. "Unidirectional spectral singularities." *Physical review letters* 113.26 (2014): 263905.
- [81] Jin, L., and Z. Song. "Incident direction independent wave propagation and unidirectional lasing." *Physical Review Letters* 121.7 (2018): 073901.
- [82] Xu, H. S., L. C. Xie, and L. Jin. "High-order spectral singularity." *Physical Review A* 107.6 (2023): 062209.
- [83] Oktay, Güneş, Mustafa Sarisaman, and Murat Tas. "Lasing with topological Weyl semimetal." *Scientific reports* 10.1 (2020): 3127.
- [84] Alomeare, Helda, Ferhat Nutku, and Mustafa Sarisaman. "Circular dichroism in nonlinear topological Weyl semimetals." *Journal of Optics* 26.6 (2024): 065502.
- [85] Ghaemi-Dizicheh, Hamed, Ali Mostafazadeh, and Mustafa Sarisaman. "Spectral singularities and tunable slab lasers with 2D material coating." *JOSA B* 37.7 (2020): 2128-2138.
- [86] Sarisaman, Mustafa, and Murat Tas. "Broadband and wide-angle invisibility with PT-symmetric 2D-Weyl semimetal." *Journal of Applied Physics* 126.16 (2019).
- [87] Sarisaman, Mustafa, and Murat Tas. "Broadband coherent perfect absorber with PT-symmetric 2D-materials." *Annals of Physics* 401 (2019): 139-148.
- [88] Jin, L., and Z. Song. "Bulk-boundary correspondence in a non-Hermitian system in one dimension with chiral inversion symmetry." *Physical Review B* 99.8 (2019): 081103.
- [89] Ota, Yasutomo, et al. "Active topological photonics." *Nanophotonics* 9.3 (2020): 547-567.
- [90] Planelles, Josep. "Axion electrodynamics in topological insulators for beginners." arXiv preprint arXiv:2111.07290 (2021).

- [91] M. A. Naimark, *Trudy Moscov. Mat. Obsc.* **3**, 181 (1954) in Russian, English translation: *Amer. Math. Soc. Transl.* (2), **16**, 103 (1960).
- [92] G. Sh. Guseinov, *Pramana J. Phys.* **73**, 587 (2009).
- [93] Xiong, Jun, et al. “Evidence for the chiral anomaly in the Dirac semimetal Na<sub>3</sub>Bi.” *Science* 350.6259 (2015): 413-416.
- [94] Liu, Z. K., et al. “Discovery of a three-dimensional topological Dirac semimetal, Na<sub>3</sub>Bi.” *Science* 343.6173 (2014): 864-867.
- [95] Desai, Dhruv C., et al. “Dominant Two-Dimensional Electron–Phonon Interactions in the Bulk Dirac Semimetal Na<sub>3</sub>Bi.” *Nano Letters* 23.9 (2023): 3947-3953.
- [96] Peng, Bo, et al. “Dirac semimetals in Sodium Ternary Compounds from Material Design on Na<sub>3</sub>Bi.” arXiv preprint arXiv:1807.01434 (2018).
- [97] Timusk, T., et al. “Three-dimensional Dirac fermions in quasicrystals as seen via optical conductivity.” *Physical Review B—Condensed Matter and Materials Physics* 87.23 (2013): 235121.
- [98] Kotov OV, Lozovik YE. “Dielectric response and novel electromagnetic modes in three-dimensional Dirac semimetal films.” *Phys Rev B* 2016;93(23).